

*Short Communication*

## **A Study on the Pitting Initiation of Duplex Stainless Steel (DSS 2205) Welded Joints Using SEM–EDS, SKPFM and Electrochemistry Methods**

Jiakun Sun<sup>1</sup>, Xiaolei Li<sup>2</sup>, Yangting Sun<sup>1</sup>, Yiming Jiang<sup>1</sup>, Jin Li<sup>1,\*</sup>

<sup>1</sup> Department of Materials Science, Fudan University, Shanghai 200433, China

<sup>2</sup> The Center of Analysis and Measurement, Fudan University, Shanghai 200433, China

\*E-mail: [corrosion@fudan.edu.cn](mailto:corrosion@fudan.edu.cn)

*Received:* 10 August 2018 / *Accepted:* 3 October 2018 / *Published:* 5 November 2018

---

The influence of laser beam welding and a subsequent short-time post-weld heat treatment on the pitting corrosion in duplex stainless steel was investigated by diverse techniques, including the polarization curve method, scanning electron microscopy–energy dispersive spectroscopy, scanning Kelvin probe force microscopy and optical microscopy. It was found that for as-welded specimens, the fused zone was the preferential pit initiation site. The Volta potential maps for the laser beam welded samples revealed that some low potential areas emerged inside the ferrite phases, which may be considered as preferential nucleation sites for the pitting corrosion. The pit morphologies showed that the pits were generated in areas with a lower surface potential value. After a 3 min post-weld heat treatment at 1080°C, the reduction in the surface potential differences indicated that the corrosion resistance of laser welded joints was restored, and the low potential areas that indicated the chromium depleted regions around the Cr<sub>2</sub>N disappeared.

---

**Keywords:** Duplex stainless steels; Laser beam welding; SKPFM; Volta potential; Pitting corrosion

### **1. INTRODUCTION**

Duplex stainless steels (DSSs) are being increasingly used in various applications and environments due to their excellent mechanical strength and corrosion resistance [1-4]. Their good properties rely on the duplex microstructure, which consists of approximately equivalent amounts of austenite ( $\gamma$ ) and ferrite ( $\alpha$ ) without other undesirable secondary phases, such as the  $\sigma$ -phase and  $\chi$ -phase [5-7]. Welding is an unavoidable fabrication process for large industrial applications of DSS. Laser beam welding (LBW) is superior to conventional arc welding process because of the low heat input, small heat affected zone (HAZ) and flexible operations. Consequently, LBW has become now

the most used welding process [8-10]. However, the very fast cooling rate for LBW causes a weld fusion zone with an unbalanced duplex phase fraction, which consists of excessive ferrite phase [11-13].

Nitrogen (N) supersaturation in the  $\alpha$ -phase is prone to occur because the solubility of N in it is much lower than for the  $\gamma$ -phase. Thus, detrimental chromium nitrides are likely to precipitate in the interior of the  $\alpha$ -phase [14-16]. Past research has indicated that the precipitation of chromium nitrides resulting from welding has a negative effect on the corrosion resistance of DSSs. Zhang et al. [17] investigated the effect of tungsten inert gas welding on the microstructure evolution and pitting corrosion behaviour of DSS. They reported that the welded zone for the as-welded metal had a higher volume fraction of the ferrite phase and some chromium-rich nitrides in the  $\alpha$ -phase. Tan et al. [3] observed that interfacial  $\text{Cr}_2\text{N}$  precipitated at the  $\alpha/\gamma$  boundary of DSS 2304 specimens during multi-pass welding simulation. As reported by Perren et al. [18], the depletion of chromium due to the formation of  $\text{Cr}_2\text{N}$  precipitates was related to a decrease in the corrosion resistance.

Post-weld heat treatment (PWHT) can eliminate that problems caused by the LBW process, such as excessive ferrite content and intermetallic phases [19-21]. Badji et al. [15] investigated the effect of PWHT in the range of 800~1150°C on the mechanical properties and microstructure of welded 2205 duplex stainless steel. They found that a PWHT temperature lower than 1100°C caused a high microhardness due to the precipitation in the  $\alpha$ -phase. Kim et al. [22] investigated the effects of PWHT and shielding gas on the pitting corrosion of DSS welds, and they reported that the pitting resistance was greatly increased due to the dissolution of  $\text{Cr}_2\text{N}$  in the  $\alpha$ -phase. In short, the literature review showed that there is a strong relationship between the PWHT parameters, microstructure and pitting corrosion behaviour of welded joints.

The ferrite phases can be easily distinguished from the austenite phases with the aid of magnetic force microscopy (MFM) on non-etched DSS surfaces [23-25]. Scanning Kelvin probe force microscopy (SKPFM) [26, 27] is a high-resolution atomic force microscopy (AFM) combined with standard Kelvin probe technology. The surface potential map, which indicates relative nobility, can be acquired simultaneously with the topography map of the metal samples [24, 28, 29]. The SKPFM maps the show the potential difference between the sample surface and the scanning reference tip with a high resolution, which is named as Volta potential [30]. Stratmann et al. [26] revealed that the Volta potential measured in air at the interface of a metal has a linear relationship with the corrosion potential measured in solution. The SKPFM has been increasingly used in the corrosion studies of metal materials recently [31]. Femenia et al. [24] reported that the Volta potential distribution over the surface of DSSs was mapped for the first time with sub-micrometre resolution by SKPFM. It was possible to associate the variation in the Volta potential with the phase boundaries and phase distribution by MFM and SKPFM mapping of the same area. According to the research of Namurata et al. [32], MFM/SKPFM were successfully applied to measure the individual phases of DSSs that had undergone a slow cooling process to precipitate a large amount of sigma phase. The sigma phase, which is not magnetic, showed a higher Volta potential than ferrite. The Volta potential variation of each phase consisting of austenite,  $\sigma$ -phase and an appreciable amount of large chromium nitrides were evaluated by SKPFM measurements [33]. The samples were isothermally aged at 800°C for six months to reach a near-equilibrium condition.

Although a number of complementary techniques have been used to describe the microstructural characteristics of DSSs at the equilibrium condition, there has been a paucity of research carried out on the characteristics of the non-equilibrium microstructure zone after welding that includes fine Cr<sub>2</sub>N precipitates. In this work, the effect of laser beam welding (LBW) was investigated without filler metal and with a subsequent short-time PWHT (annealed at 1080°C for 3 min) on the microstructure evolution and pitting corrosion behaviour of duplex stainless steel, DSS 2205. Scanning electron microscopy–energy dispersive spectroscopy (SEM-EDS) analysis was combined with MFM/SKPFM. The MFM was applied to identify the ferrite and austenite phase distribution without surface etching, while SKPFM was used to study the relative nobility of the different phases. Potentiodynamic polarization was applied to study the pitting initiation of LBW DSS in 1.0 mol/L NaCl solution. In addition, whether the surface potential (SP) values of the weaker phase (where “weaker” means “less resistant”) served as a criterion for ranking pitting resistance, or not, was verified through microstructural observations after electrochemistry tests.

## 2. EXPERIMENTAL

### 2.1. Material and sample preparation

The DSS 2205 plates with a 1.5 mm thickness were obtained from the Baosteel Technology Center. The chemical compositions of the experimental DSS 2205 are given in Table 1. An autogenous LBW procedure was used to fabricate the joints without filler metal and the corresponding welding parameters are listed in Table 2.

**Table 1.** Chemical composition of DSS 2205 (wt.%)

Materials	C	Si	Mn	S	P	Cr	Ni	Cu	N	Mo	Fe
2205	0.021	0.46	1.52	0.001	0.008	22.36	5.72	0.069	0.17	3.02	Bal.

**Table 2.** Laser welding parameters used in the experiment[35]

Laser beam configuration	Unit	Value
Laser power	W	1500
Travel speed	Mm/min	2000
Spot size on surface	Mm <sup>2</sup>	1.5×1.5
Focal position	-	At specimen surface
Deviation distance to focus spot	Mm	0
Shielding gas flow rate (Ar)	L/min	15
Backing gas flow rate (Ar)	L/min	15

The short-time PWHT was performed for 3 minutes at 1080°C in a muffle furnace in an N<sub>2</sub> atmosphere and then the samples were quenched in cold water. The fusion zone and the heat-affected zone were included in the specimens, which were cut from the joint area with a dimension of 12mm×12mm×1.5mm for electrochemical tests and microscopy examination. Prior to each experiment, the test sample was ground mechanically using successive grades of emery paper up to 2,000 grit. They were then polished with diamond pastes of 1.5µm, degreased with ethanol, rinsed with distilled water and then blow-dried [34]. The specimens serving as working electrodes were embedded in an epoxy resin with an exposure area of 1 cm<sup>2</sup>. The interfaces between the specimen and resin were sealed with a special silica gel sealant to avoid crevice corrosion. Metallographic specimens were observed by optical microscopy (OM) and scanning electronic microscopy (Phillips XL30 FEG SEM) after etching in a 30 wt% KOH electrolyte.

## 2.2 SKPFM Measurement

The MFM and SKPFM measurements were performed with a Dimension Icon™ Nanoscope V AFM from Bruker Instruments Inc. The AFM instrument was placed in an ISO class 3 cleanroom, according to standard ISO 14644-1, and the measurements were made in air in the lab with room temperature of 23°C -25°C and relative humidity around 40%. The tips used were Bruker™ SPM tips, specifically the MESP type, with a length of 200-250 µm and resonant frequency of 60-100 kHz for the MFM measurements. The SCM-PIT type with the same length and resonant frequency were used for SKPFM measurements.

A dual-pass mode was frequently used to map the topography and Volta potential of the metal samples. The topographical data was recorded during the first scan with tapping mode. After the first scan, the tip was lifted up to minimize the influence of the topography during the second scan that records the Volta potential for the same surface area. The topographical signal was added to the lift height to maintain the tip-sample distance during the second scan. In the new generation SKPFM, the simultaneous mapping of the Volta potential and topography was done without lifting through the multi-frequency measurements.

## 2.3 Electrochemical measurements

All the electrochemical measurements were conducted using a potentiostat workstation PARSTAT2273 collected to a three-electrode cell. A saturated calomel electrode (SCE) and a platinum foil were used as the reference and auxiliary electrode, respectively. Unless otherwise stated in this paper, all potentials recorded were referred to SCE. The test solution, 1 mol/L NaCl, was made up from analytical grade reagents and distilled water. Before the test, the electrolyte was bubbled with pure nitrogen gas for at least 30 min to get rid of the oxygen gas.

The sample was used in potentiodynamic polarization measurements at 60°C ±1°C with a scan rate of 0.1667 mV/s. The scan started from -400 mV (lower than the open circuit potential) to the potential where the current indicated that stable pitting started. The pitting potential (E<sub>p</sub>) was reported

as the potential at which the current density exceeded  $100 \mu\text{A}/\text{cm}^2$  [36]. In addition, prior to the potentiodynamic polarization measurements, the working electrode was cathodically polarized at  $-900 \text{ mV}$  for  $300 \text{ s}$  in order to deoxidize the surface of the specimens. This was done to improve the reproducibility of the experiment, and it was allowed to stabilize at the open circuit potential for  $10 \text{ min}$  [37]. Each electrochemical test was performed thrice and the results were found to be consistent and reproducible.

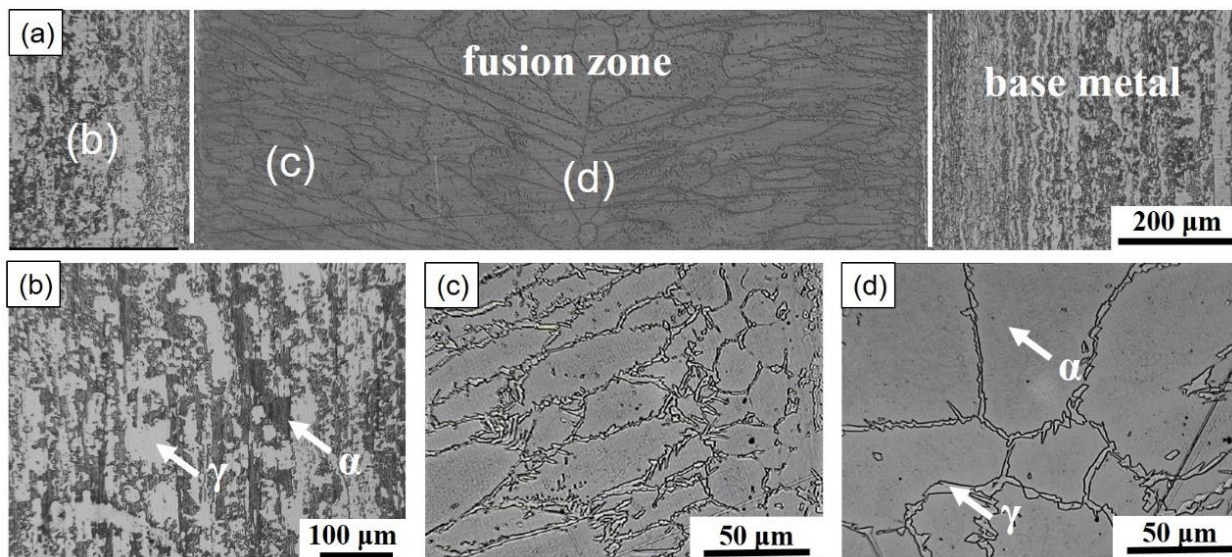
Based on the results of the potentiodynamic polarization measurements, the next experiment was done potentiostatically at a certain anodic potential that was well above the pitting potential. The specimen was allowed to rest for  $120 \text{ s}$  at the polarization potential until the appearance of the pitting corrosion. After the electrochemical measurements, the morphologies of the pitting corrosion were observed by light OM and SEM

### 3. RESULTS AND DISCUSSION

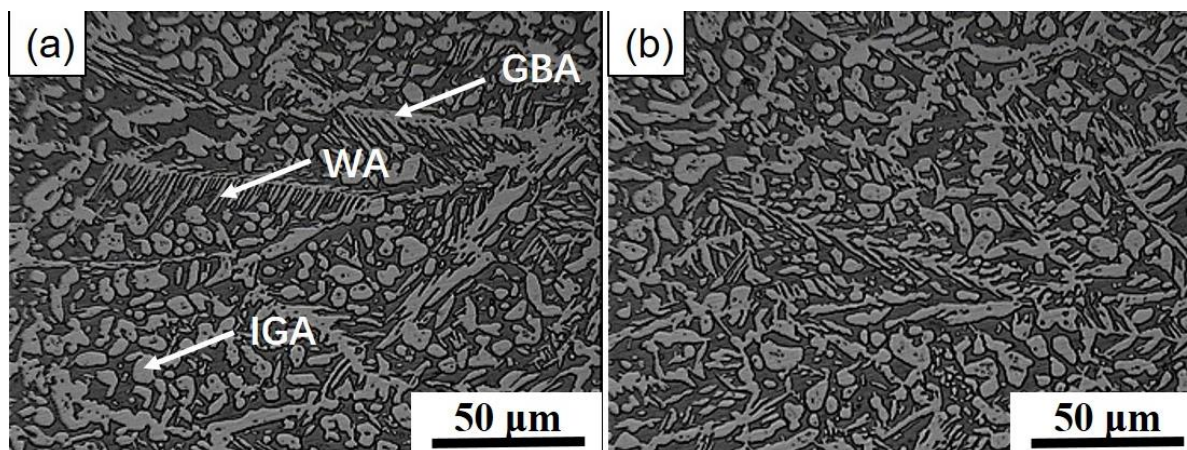
#### 3.1 Microstructural observation

Figure 1 shows the morphologies of different zones of the DSS 2205 LBW as-welded joint. Figure 1(a) illustrates the microstructure of a typical LBW joint. A narrow fusion zone (FZ), about  $1 \text{ mm}$  wide, was clearly observed, but the HAZ was hardly identified. Figures 1(b), 1(c) and 1(d) correspond to the area marked with the same letter as Fig. 1(a), respectively. Figure 1(b) shows the optical duplex microstructure of the base metal. It indicates that the white and island-like  $\gamma$  phase was embedded in the continuous grey ferrite phase matrix without visible precipitates. Figure 1(c) shows the edge of the FZ, which consists of columnar ferrite grains that grew epitaxially towards the centre of the FZ. Figure 1(d) shows the centre of the FZ, where equiaxed ferrite grains were found [17]. It also could be seen that the average  $\alpha$ -phase volume fraction was extremely high in the FZ. The  $\alpha$ -phase was the only phase formed directly from the liquid, and the ferrite-to-austenite transformation occurred subsequently in the solid state in the temperature range of  $800^\circ\text{C}$  -  $1200^\circ\text{C}$  [38]. Also, a longer time cannot be given for the transformation from the  $\alpha$ -phase to the  $\gamma$ -phase [39]. The grain boundary austenite (GBA), which is light in the Figs. 1(c) and (d), was initially formed at the boundaries of the ferrite grains. The Widmanstätten austenite (WA) along the ferrite grain boundaries began to grow into the interior and a little intragranular austenite (IGA) appeared within the ferrite grains. The amount of WA and IGA was very small. All three kinds of austenite are clearly shown in Figs. 1(c) and (d).

Figure 2 shows the microstructure change for the DSS 2205 LBW joints after  $3 \text{ min}$  PWHT at  $1080^\circ\text{C}$ . The post-weld heat treatment can stimulate the Widmanstätten austenite and intragranular austenite to appear and grow. Compared with the as-welded condition shown in Figs. 1(c) and (d), the amount of WA and IGA was clearly greater.



**Figure 1.** Optical micrographs of as-welded DSS 2205 joints etched by 30 wt.% KOH solution: (a) joints, (b) base metal, (c) enlarged edge of fusion zone and (d) centre of fusion zone.



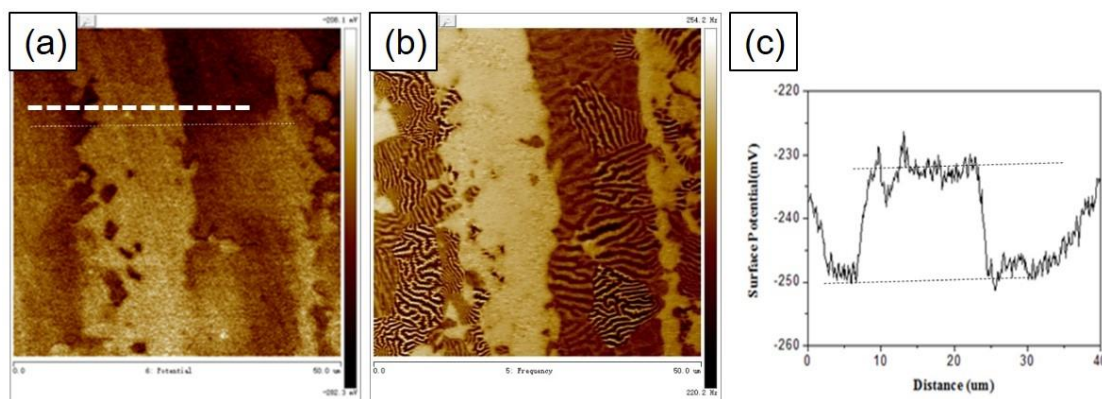
**Figure 2.** Microstructure of the (a) central region and (b) edge of LBW fusion zone after 3 min PWHT at 1080°C.

### 3.2 SKPFM Measurement

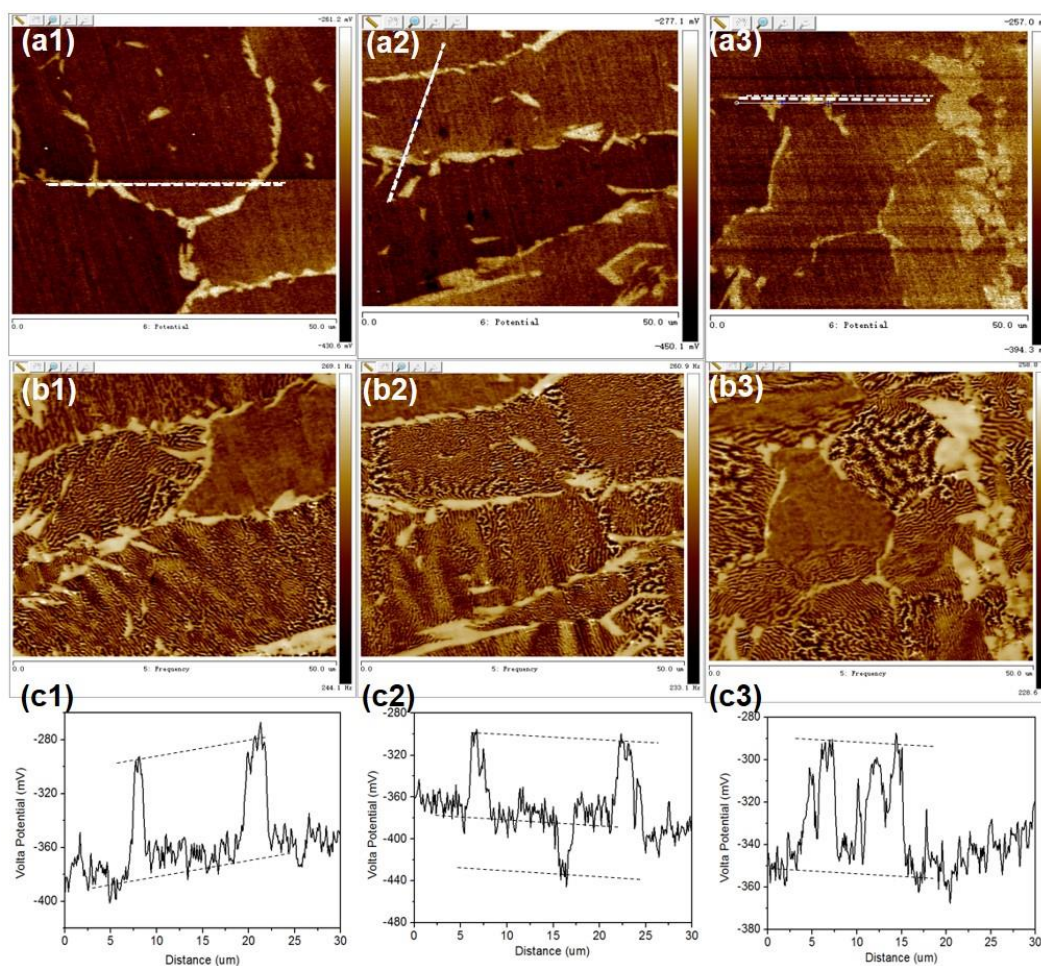
#### 3.2.1 MFM/SKPFM mapping and Volta potential variation

The magnetic domain distribution, the Volta potential map and a Volta potential line profile of the base metal were measured over the polished surface (50 mmx50 mm) on the same area, as shown in Fig. 3. It was not shown here since the topography map does not provide any essential information. A lower Volta potential (darker in the map) was observed for the ferrite phase, and a higher Volta potential (lighter in the map) was observed for the austenite phase. The austenite phase was rather uniform, whereas the ferrite phase appeared striped due to the magnetic domains. Figure 3(a) shows different crystallographic and domain orientations within the ferrite phase [25]. The average potential difference between the ferrite phase and austenite phase in Fig. 3(c) was approximately  $20 \pm 2$  mV. A

higher Volta potential for the austenite phase indicates that the austenite was nobler than the ferrite in the base metal. The Volta potential difference observed here could indicate a certain corrosion tendency between the two phases [32].



**Figure 3.** (a) SKPFM image, (b) MFM image, and (c) Volta potential profile of a line as indicated in (a) on the same surface area of the base metal 2205.



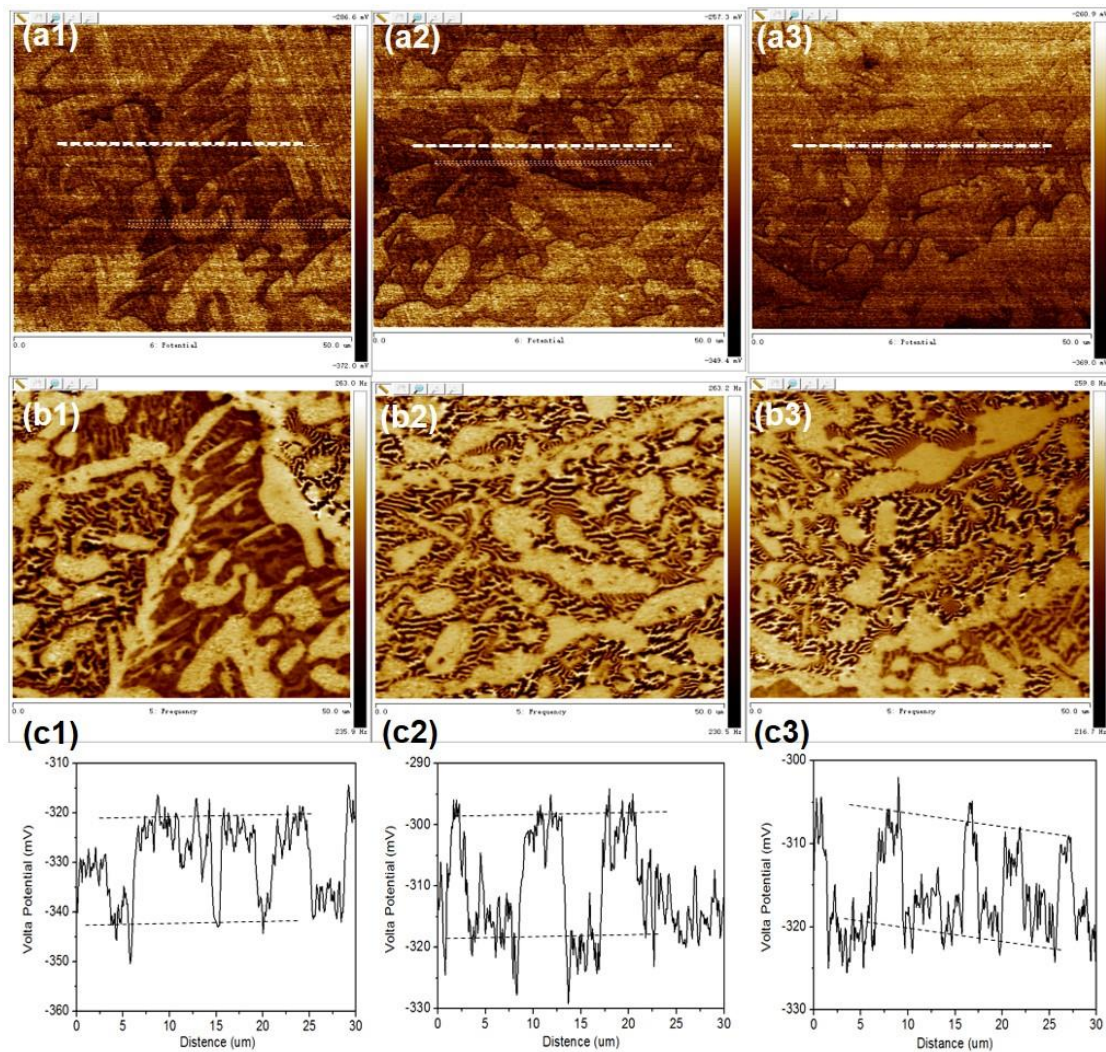
**Figure 4.** (a1) (a2) (a3) SKPFM, (b1) (b2) (b3) MFM images of the fusion zone of the welded joint and (c1) (c2) (c3) Volta potential difference profile of a line as shown in (a1) (a2) (a3).

Figure 4 shows the Volta potential map, magnetic domain distribution and Volta potential line profile for the fused zone in the DSS 2205 LBW as-welded joint. The austenite exhibited a higher Volta potential than the ferrite and appeared brighter on the map. To cover the entire FZ, three individual scanning steps ( $50\mu\text{m}\times 50\mu\text{m}$ ) were accomplished. Imaging was performed by sweeping from the central region to the edge of the FZ. Equiaxial ferrite grains were observed at the enlarged centre part of FZ, as shown in Fig. 4(a1). The columnar ferrite grains were observed growing towards the centre of the FZ and were driven by temperature gradient, as shown in Figs. 4(a2) and 4(a3). The average data from at least five line profiles that were measured in each region gave the surface potential difference to be 76.5 mV for region (a1), 67 mV for region (a2) and 56 mV for the region (a3), as illustrated in Table 3. It is worth noting that some round areas had the lowest Volta potential that emerged from inside the ferrite phases in region (a2) and led to the weakest pitting resistance. This will be discussed below.

**Table 3.** Volta potential differences between  $\delta$  phase and  $\gamma$  phase from Volta potential profile analyses (average of at least five line analyses) from region a1, a2 and a3 in the FZ.

	BM	a1	a2	a3	Average(a1,a2,a3)
$\Delta\text{SP}(\delta-\gamma)/\text{mV}$	18	76.5	67(129)	56	66.5

Figure 5 shows the Volta potential map, magnetic domain distribution and a Volta potential line profile from the polished surface ( $50\mu\text{m}\times 50\mu\text{m}$ ) for the DSS 2205 LBW joint after 3 min PWHT at  $1080^\circ\text{C}$ . The imaging was performed by sweeping from the central region to the edge of the FZ. As previously stated, the darker areas in the image are the ferrite phase, which had a lower Volta potential, and the lighter areas are the austenite phase, which was a higher Volta potential. The non-magnetic WA (austenite formed as Widmanstätten sideplates grown into ferrite grains) could be seen primarily at the boundaries of the austenite/ferrite phases. Note that there were no round precipitates in the region of the FZ. Figures 5(b1), 5(b2) and 5(b3) show the magnetic domain distribution in the same area corresponding to Figs. 5(a1), 5(a2) and 5(a3). In these figures, the ferromagnetic ferrite is striped and the paramagnetic austenite has a uniform appearance. The average potential difference between austenite and ferrite from at least five line analyses (e.g. Figs. 5(c1), 5(c2) and 5(c3)) was approximately  $20 \pm 4$  mV. Compared with the as-welded specimens, all the regions in the heat-treated specimens had lower surface potential differences, which indicated the beneficial effect of short-time PWHT. It could be noticed that the Volta potential difference between the austenite and ferrite was almost equal for the PWHT sample and the base metal. It was clear evidence that the weld joint annealed 3 min at  $1080^\circ\text{C}$  repaired the adverse impact on the pitting corrosion during welding.



**Figure 5.** (a1) (a2) (a3) SKPFM, (b1) (b2) (b3) MFM images of the fusion zone of welded joint after PWHT and (c1) (c2) (c3) Volta potential difference profile of a line as shown in (a1) (a2) (a3)

### 3.2.2 the precipitation in the ferrite of the fusion zone of welded joint

Some round areas were recognized with lowest Volta potential emerging inside the ferrite phases of the fusion zone, as shown in Fig. 4. The surface potential difference between the austenite phase and the lowest Volta potential area was 129 mV, as shown in Table 4. On account of the linear relationship between the Volta potential and the corrosion potential in solution [26], the low-potential areas were most likely connected with the lost pitting corrosion resistance caused by laser beam welding.

It was reported that chromium nitrides form in the HAZ and FZ due to the influence of welding thermal cycle of DSS [3]. A TEM analysis of the as-welded UNS S31803 duplex stainless steel indicated that all precipitates observed in the weld joint were  $\text{Cr}_2\text{N}$  precipitates [35]. Nevertheless,  $\text{Cr}_2\text{N}$  precipitates was too small to show any contrast in the Volta potential map. It was convincing that the lowest Volta potential area indicated the chromium depleted regions around  $\text{Cr}_2\text{N}$ , as shown in Fig.

6(a). Figure 6(b) shows the morphologies of the as-welded joint that were etched by oxalic acid. Small pits occurred within the ferrite phase and indicated the presence of  $\text{Cr}_2\text{N}$  precipitation (arrow marks)[40].

The nitrides were more likely to precipitate in the ferrite phase because of the solubility of nitrogen in the ferrite decreased rapidly with the sharp decrease in temperature [6, 8, 41, 42]. The preferential pitting corrosion could initiate in these areas, as supported by the potentiodynamic polarization tests that would be discussed later.

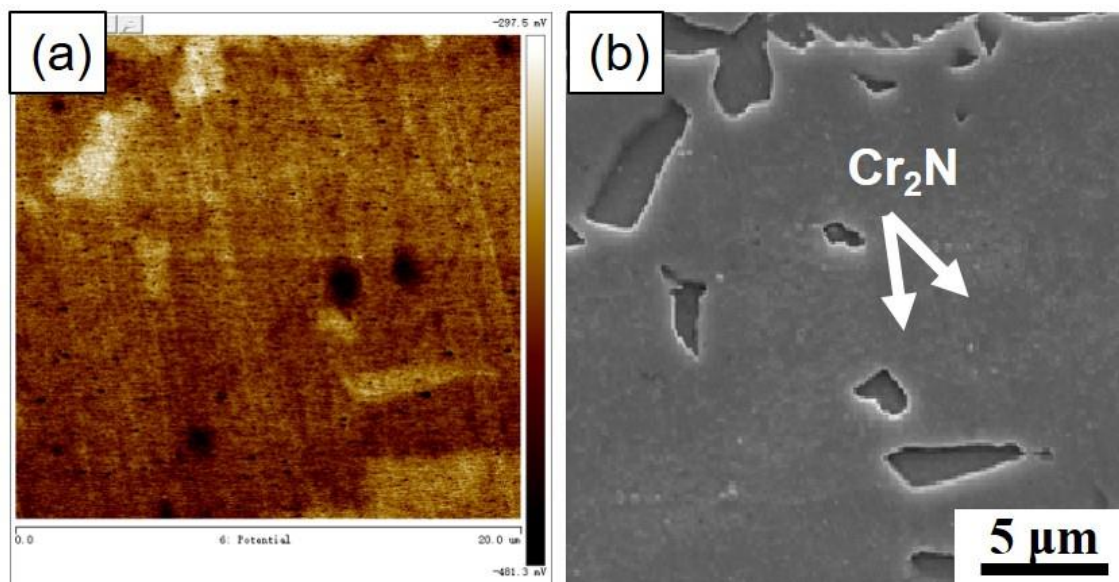


**Figure 6.** (a) SKPFM image, (b) surface morphology of as-welded joint observed by SEM after etched by 10% oxalic acid

### 3.3 Electrochemical measurement

The potentiodynamic anodic polarization technique was used to evaluate the effect of LBW and a 3 min PWHT at  $1080^\circ\text{C}$  on the pitting corrosion resistance of DSS 2205. Figure 7 shows the representative polarization curves of the specimens exposed to 1 mol/L NaCl solution. The corrosion electrochemical parameters are listed in the Table 4. As can be seen, the test curves were characterized by a passive region, where the current density gradually stabilized. The passivation current density ( $i_p$ ) for the LBW specimen was higher than for the PWHT and as-received specimens. The polarization curves revealed that the post-weld heat treatment affected the passivation properties of the steel. The pitting potential ( $E_p$ ) obtained after 3 min PWHT at  $1080^\circ\text{C}$  was close to the  $E_p$  value for the as-received base metal, and it was also higher than the LBW specimen. The weld increased the susceptibility of the steel to localized corrosion. The reduction of the passive potential range and the increase of the passivity current density could be attributed by the presence of  $\text{Cr}_2\text{N}$  precipitation in the FZ, as shown in the microstructure of Fig. 6. This suggested that the welded joint annealed 3 min at  $1080^\circ\text{C}$  regained the lost pitting corrosion resistance during welding, which is consistent with the SKPFM measurement.

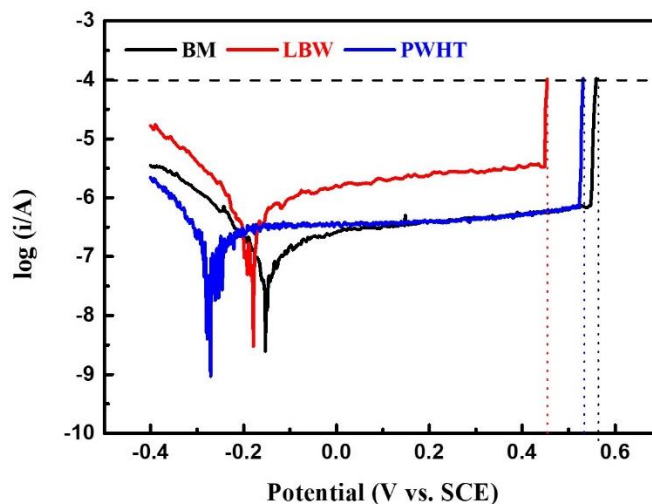


**Figure 7.** Polarization curves obtained for DSS 2205 in 1 mol/L NaCl solution.

**Table 4.** Passivation current density and pitting potential of DSS 2205 in 1 mol/L NaCl solution

Sample	Passivation Current Density ( $i_p$ ) (A/cm <sup>2</sup> )	Pitting Potential( $E_p$ ) (V)
Base metal	3.9903E-07	0.559
LBW	2.3878E-06	0.454
PWHT	3.9174E-07	0.531

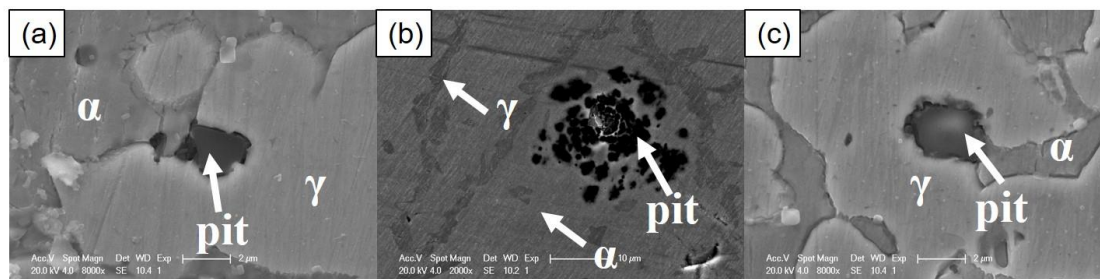


**Figure 8.** Pit morphologies after potentiostatic measurements: (a) as-received DSS 2205 base metal, (b) as-welded specimen; (c) as-welded specimen with PWHT

After measuring the polarization curves, an additional experiment was done potentiostatically at a fixed anodic potential of 0.6V (vs. SCE) for 90 s to investigate the pitting corrosion resistance. The chosen potential of 0.6 V (vs. SCE) was above the pitting potential of three kinds specimens. Figure 8(a) shows the as-received DSS 2205 base metal, in which the pitting corrosion initiated predominantly in the ferrite phase. Comparing with as-received specimens, pits on the as-welded specimens were larger and possibly occurred more in the FZ (Figure 8(b)). Similar to the as-received specimen, the pitting also occurred at the ferrite phase in the base metal for the PWHT, as seen in Figure 8(c).

It was concluded that a short-time PWHT was necessary to improve the pitting corrosion resistance of the LBW joint. When combined with the former research results, it was found that the

mechanism of pitting corrosion was the selective dissolution of the ferrite phase in the FZ [35]. The occurrence of pits in the FZ indicated that the FZ with an excessive content of Cr<sub>2</sub>N precipitation was less resistant. Therefore, it is important to improve the corrosion resistance of the FZ with the appropriate PWHT process.

#### 4. CONCLUSIONS

In this work, the influence of LBW and PWHT on the corrosion behaviour of DSS 2205 was investigated by SEM/EDS, SKPFM/MFM and electrochemical tests. The following conclusions can be drawn:

1. For the first time, the SKPFM/MFM measurement was used to investigate the initiation of pitting corrosion on LBW DSS. The paramagnetic austenite phase showed a higher Volta potential compared with the ferromagnetic ferrite phase and led to a higher corrosion resistance. A local Volta potential drop at the phase boundaries was clearly observed in the FZ.

2. The as-welded DSS 2205 samples exhibited a severely impaired pitting corrosion resistance, as the Volta potential difference increased from 18mV (base metal) to 66.5mV (FZ). In the FZ, some low-potential areas emerged from inside the ferrite phases and were determined to be pitting nucleation sites. Stable pits occurred preferentially at the  $\alpha$ -phase in the FZ due to the unbalanced microstructure and the Cr-depleted zone induced by Cr<sub>2</sub>N precipitation.

3. After 3 min PWHT at 1080°C, more austenite was formed in FZ and the Volta potential difference between the austenite phase and ferrite phase decreased to 20mV (fuse zone). This was an indication of the improved corrosion resistance of the welded joint. The electrochemical measurement confirmed such a conclusion.

#### ACKNOWLEDGEMENTS

The authors would like to thank Li Li, professor of the center of analysis and measurement, for her assistance, whilst they gratefully acknowledge the helpful collaboration of Baosteel. This work was supported by the National Key Research and Development Program of China (No. 2018YFB 0704400), National Natural Science Foundation of China under Grants No. 51671059 and 51501041, and the key laboratory of space launching site reliability technology.

#### References

1. L. Chen, H. Tan, Z. Wang, J. Li, Y. Jiang, *Corros. Sci.*, 58 (2012) 168.
2. B. Deng, Z. Wang, Y. Jiang, T. Sun, J. Xu, J. Li, *Corros. Sci.*, 51 (2009) 2969.
3. H. Tan, Z. Wang, Y. Jiang, Y. Yang, B. Deng, H. Song, J. Li, *Corros. Sci.*, 55 (2012) 368.
4. L.F. GarfiasMesias, J.M. Sykes, C. Tuck, *Corros. Sci.*, 38 (1996) 2267.
5. Z. Cvijovic, G. Radenkovic, *Corros. Sci.*, 48 (2006) 3887.
6. H.Y. Liou, R.I. Hsieh, W.T. Tsai, *Mater. Chem. Phys.*, 74 (2002) 33.
7. Y. Sun, X. Wu, X. Wu, J. Li, *Int J. Electrochem Sc*, 11 (2016) 9666.
8. J. Nowacki, P. Rybicki, *J. Mater. Process. Tech.*, 164 (2005) 1082.
9. Y. Guo, T. Sun, J. Hu, Y. Jiang, L. Jiang, J. Li, *J. Alloy. Compd*, 658 (2016) 1031.
10. J.O. Nilsson, T. Huhtala, P. Jonsson, L. Karlsson, A. Wilson, *Metall. Mater. Trans. A.*, 27 (1996)

2196.

11. D.E. Nelson, W.A. Baeslack, J.C. Lippold, *Weld. J.*, 66 (1987) S241.
12. T. Ogawa, T. Koseki, *Weld. J.*, 68 (1989) S181.
13. N. Sridhar, L.H. Flasche, J. Kolts, *Mater. Performance*, 23 (1984) 52.
14. C.M. Garzon, A.J. Ramirez, *Acta Mater.*, 54 (2006) 3321.
15. R. Badji, M. Bouabdallah, B. Bacroix, C. Kahloun, B. Belkessa, H. Maza, *Mater. Charact.*, 59 (2008) 447.
16. M. Yousefieh, M. Shamanian, A. Saatchi, *J. Iron Steel Res. Int.*, 18 (2011) 65.
17. Z. Zhang, Z. Wang, Y. Jiang, H. Tan, D. Han, Y. Guo, J. Li, *Corros. Sci.*, 62 (2012) 42.
18. R.A. Perren, T. Suter, C. Solenthaler, G. Gullo, P.J. Uggowitzer, H. Bohni, M.O. Speidel, *Corros. Sci.*, 43 (2001) 727.
19. H. Liu, X. Lu, X. Jin, *Mater. Design*, 32 (2011) 2269.
20. Z. Zhang, H. Jing, L. Xu, Y. Han, L. Zhao, X. Lv, J. Zhang, *J. Manuf Process*, 31 (2018) 568.
21. M.A. Mohammed, K.A. Shrikrishna, P. Sathiya, *Mater. High Temp.*, 35 (2018) 309.
22. S. Kim, S. Jang, I. Lee, Y. Park, *Corros. Sci.*, 53 (2011) 1939.
23. A. Dias, M.S. Andrade, *Appl. Surf. Sci.*, 161 (2000) 109.
24. M. Femenia, C. Canalias, J. Pan, C. Leygraf, *J. Electrochem. Soc.*, 150 (2003) B274.
25. N. Sathirachinda, R. Gubner, J. Pan, U. Kivisakk, *Electrochemical. Solid ST*, 11 (2008) C41.
26. M. Stratmann, *Corros. Sci.*, 27 (1987) 869.
27. S.G. Yee, R.A. Oriani, M. Stratmann, *J. Electrochem. Soc.*, 138 (1991) 55.
28. V. Guillaumin, P. Schmutz, G.S. Frankel, *J. Electrochem. Soc.*, 148 (2001) B163.
29. E. Rahimi, A. Rafsanjani-Abbasi, A. Imani, S. Hosseinpour, A. Davoodi, *Corros. Sci.*, 140 (2018) 30.
30. H.O. Jacobs, H.F. Knapp, A. Stemmer, *Rev. Sci. Instrum.*, 70 (1999) 1756.
31. C. Ornek, P. Reccagni, U. Kivisakk, E. Bettini, D.L. Engelberg, J. Pan, *Int. J. Hydrogen Energ.*, 43 (2018) 12543.
32. N. Sathirachinda, R. Pettersson, J. Pan, *Corros. Sci.*, 51 (2009) 1850.
33. N. Sathirachinda, R. Pettersson, S. Wessman, J. Pan, *Corros. Sci.*, 52 (2010) 179.
34. B. Deng, Y. Jiang, J. Liao, Y. Hao, C. Zhong, J. Li, *Appl. Surf. Sci.*, 253 (2007) 7369.
35. Y. Yang, Z. Wang, H. Tan, J. Hong, Y. Jiang, L. Jiang, J. Li, *Corros. Sci.*, 65 (2012) 472.
36. L. Zhang, Y. Jiang, B. Deng, W. Zhang, J. Xu, J. Li, *Mater. Charact.*, 60 (2009) 1522.
37. J. Gao, Y. Jiang, B. Deng, Z. Ge, J. Li, *Electrochim. Acta*, 55 (2010) 4837.
38. Y. Yang, B. Yan, J. Li, J. Wang, *Corros. Sci.*, 53 (2011) 3756.
39. I. Gilath, J.M. Signamarcheix, P. Bensussan, *J. Mater. Sci.*, 29 (1994) 3358.
40. A.M. ElBatahy, *Mater. Lett.*, 32 (1997) 155.
41. J.O. Nilsson, A. Wilson, *Mater. Sci. Tech.-Lond*, 9 (1993) 545.
42. H. Ha, H. Kwon, *Electrochim. Acta*, 52 (2007) 2175.